Experimental observation and numerical investigation of filamentary structures in magnetized plasmas

Cite as: Phys. Plasmas **27**, 022101 (2020); https://doi.org/10.1063/1.5135761
Submitted: 08 November 2019 . Accepted: 07 January 2020 . Published Online: 03 February 2020

Mohamad Menati, Behnam Rasoolian, Edward Thomas, and Uwe Konopka

Physics of Plasmas ARTICLE scitation.org/journal/php

Experimental observation and numerical investigation of filamentary structures in magnetized plasmas

Cite as: Phys. Plasmas **27**, 022101 (2020); doi: 10.1063/1.5135761
Submitted: 8 November 2019 · Accepted: 7 January 2020 ·
Published Online: 3 February 2020

Mohamad Menati,[1,a)] Behnam Rasoolian,[2,b)] Edward Thomas,[1,b)] and Uwe Konopka[1,b)]

AFFILIATIONS

[1]Department of Physics, Auburn University, Auburn, Alabama 36832, USA
[2]Department of Computer Science and Software Engineering, Auburn University, Auburn, Alabama 36849, USA

[a)]**Author to whom correspondence should be addressed:** mzm0085@auburn.edu
[b)]**Electronic addresses:** bzr0014@auburn.edu; etjr@auburn.edu; and uzk0003@auburn.edu

ABSTRACT

Filamentary structures in low-pressure, low-temperature plasmas are produced when strong magnetic fields are applied parallel to the electric field defined by parallel electrodes. Filamentary structures are regions within the plasma that have distinct properties such as optical brightness and extend along the magnetic field lines. In our experiments, an argon, radio frequency discharge is exposed to a strong background magnetic field in the magnetized dusty plasma experiment at Auburn University. Different forms of filamentary structures emerge in the plasma such as columns, target, or spiral-like structures. To investigate the origin and the characteristics of these patterns, we have developed a three-dimensional fluid model that can reproduce the experimental observations which enables us to investigate the underlying mechanisms of the filamentation process.

I. INTRODUCTION

Pattern formation and self-organization have been observed in a variety of natural and laboratory systems.[1–11] In plasma systems, self-organized patterns have been observed in arc discharges,[12–17] glow discharges,[18–20] streamers,[21–23] and dielectric barrier discharges.[24–26] Plasma environments that produce self-organized patterns often have large aspect ratios, the width to the plasma exceeds its height, suggesting that plasma-surface interactions play a dominating role.[27] In a magnetized plasma, the motion of the charged components is further limited across the magnetic field lines, increasing the effective aspect ratio of the plasma. In this way, the presence of magnetic field in electric discharges can support the formation of self-organized structures. The presence of the magnetic field can also stimulate instabilities that in return can lead to the formation of self-organized patterns. Kent[28] performed experiments and modeling of self-organization triggered by a transverse Kelvin–Helmholtz instability in a Q-machine. Also, shear-flow instability in plasmas under the influence of strong magnetic field can lead to vortex or spiral structure formation.[29,30] Driscoll *et al.*[31] reported on how relaxation of a 2D turbulence in a magnetized electron column can develop filamentary structures.

Multiple numerical and analytical models have been developed to explain pattern formation in magnetized plasmas. Evolution and saturation of Kelvin–Helmholtz instabilities at the interface of a shear flow configuration in the presence of parallel and antiparallel magnetic fields have been investigated by Keppens *et al.*[32] Kono *et al.*[33,34] analytically reproduced the formation of spiral and vortexlike structures in magnetized rotating plasmas and electron gases based on linear Eigenfunctions. Trelles[35,36] explained the formation of self-organized anode patterns in arc discharges using numerical simulations and showed that the degree of thermodynamic nonequilibrium and thermal instability play the main role in this type of pattern formation.

Filamentation and pattern formation have been also observed in low-temperature radio frequency (RF) plasmas having a high magnetic field. The first observations of the phenomena were reported by Konpoka *et al.*,[37] and it was further studied by Schwabe *et al.*[38] and Bandyopadhyay *et al.*[39] Filaments were observed as optically bright, elongated structures that formed parallel to the magnetic field. Aspects of pattern formation in RF-plasmas have been investigated as a function of pressure and magnetic field strength. More recent experiments

using the magnetized dusty plasma experiment (MDPX) at Auburn University[40] have confirmed a number of the earlier observations.

Pattern formation has been observed in low-temperature magnetized discharges (electron temperatures of few electron volts and room temperature ions) at pressures below 50 Pa. These patterns can be stationary or dynamic exhibiting strong dependency on pressure and magnetic field strength. The shape and behavior of the patterns vary with pressure. By increasing pressure, the patterns alter from discrete filaments to continuous patterns and disappear at high pressures.[38] Also, patterns appear in the plasma at different magnetic field thresholds that depend on discharge power, gas type, and neutral gas pressure. For instance, in an argon plasma at a pressure of 10 Pa and plasma density of 10^{15} m^{-3}, this magnetic field threshold is on the order of 1 T.

In the current work, we present recent experimental observations of pattern formation and filamentation in low-pressure/low-temperature discharges and discuss their variation with applied power and conductivity of the electrodes. We also introduce a numerical three-dimensional (3D) plasma fluid model to investigate the phenomena. In this model, perturbations in electron and ion densities are introduced to the background plasma in the presence of a high magnetic field to initiate the filamentary structures.

The reminder of this paper is organized as follows: In Sec. II, we present recent observations from experiments on the MDPX device. Section III introduces our numerical approach for the 3D model and discusses our initial results in the context of experimental observations. Finally, Sec. IV will give a summary and outlook of the work.

II. EXPERIMENTAL SETUP AND OBSERVATIONS

The experiments were performed in the octagonal vacuum chamber of MDPX at Auburn University.[41] The chamber uses a pair of parallel plate electrodes which are 30.5 cm in diameter and separated by 63 mm to generate a capacitively coupled plasma (CCP). The bottom electrode is grounded while the top electrode is powered at an RF frequency of 13.56 MHz. A background magnetic field is applied, oriented perpendicular to the electrodes. The plasma is observed through a 15 cm diameter view port at the top of the vacuum chamber. A schematic drawing and an actual picture of MDPX device are shown in Fig. 1.

When viewed from the top, the self-organized structures in the plasma can appear as discrete bright spots, circular, and even spiral-like patterns as shown in Figs. 2–4. Filamentary structures are persistent phenomena, only slowly varying in time (0.1 s to 10's of seconds), which makes them long-lived compared to the typical time scales of ion or electron phenomena

$$\Delta t_{\text{filamentation}} \gg \frac{1}{\omega_{p\alpha}}, \frac{1}{\omega_{c\alpha}}, \tag{1}$$

where $\omega_{p\alpha}$ and $\omega_{c\alpha}$ are the electron or ion plasma and cyclotron frequencies.

To investigate the effect of the plasma density on filamentation, the discharge power was varied from 0.40 to 4.03 W, while keeping the gas pressure (argon) at 4.7 Pa and the magnetic field at 0.77 T constant. The resulting measurements are presented in Figs. 2(a)–2(e). These results show that the homogeneity of the plasma increases; therefore the filamentation dissipates as the discharge power and

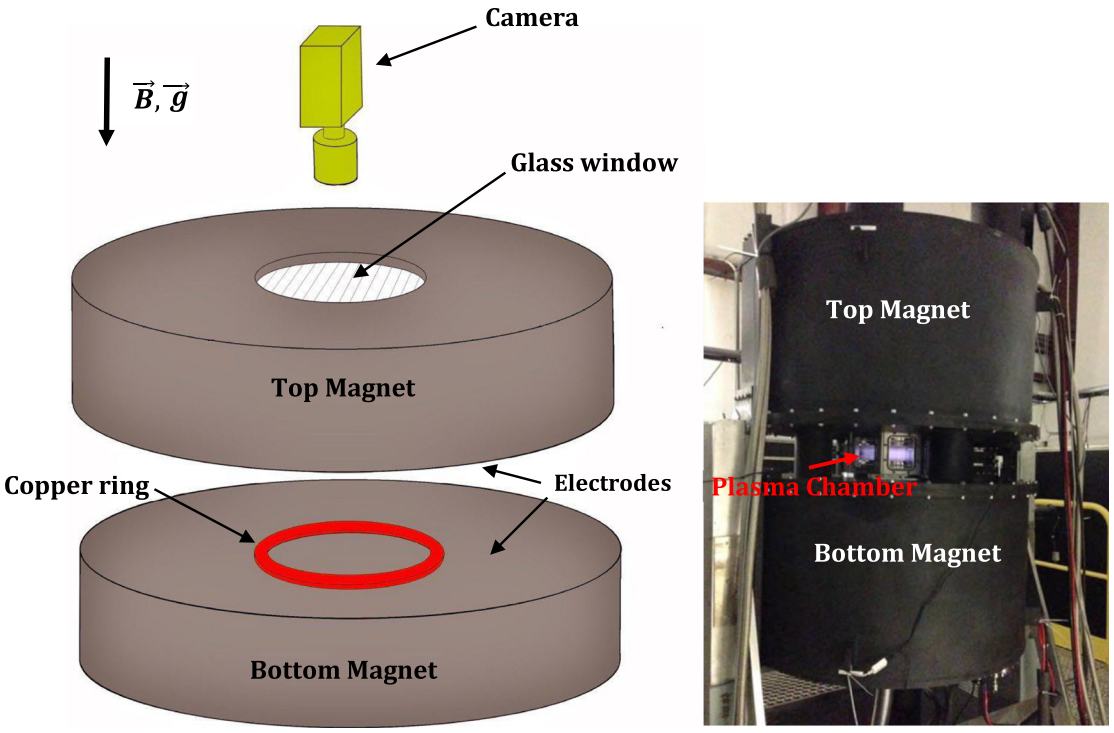

FIG. 1. Schematic drawing and actual picture of the MDPX device at Auburn University which consists of two superconducting magnets and an octagon plasma chamber.

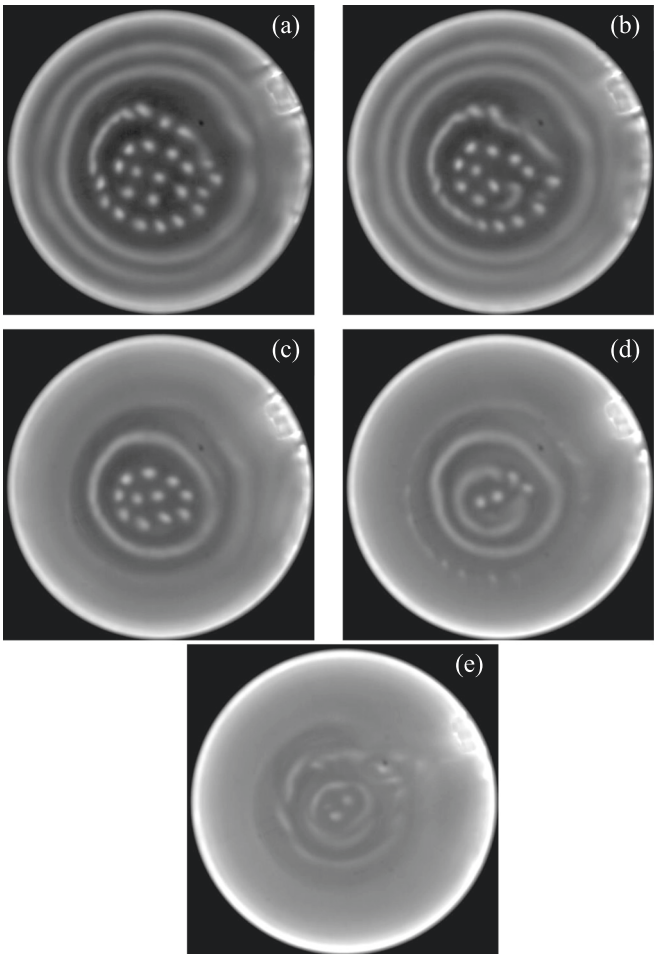

FIG. 2. Top view of pattern formation in an RF argon plasma at a neutral pressure of 4.7 Pa, magnetic field of 0.77 T, and varying discharge powers. (a) 0.4 W, (b) 0.85 W, (c) 1.5 W, (d) 2.32 W, and (e) 4.03 W.

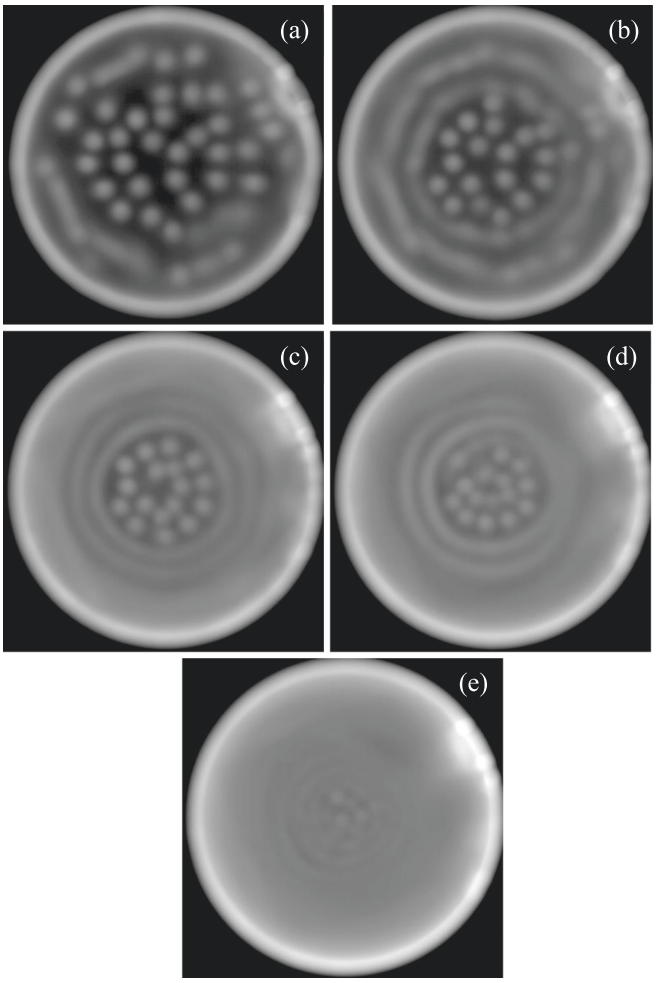

FIG. 3. Top view of a patterned RF argon plasma at a neutral pressure of 4.7 Pa with a glass plate placed on the lower electrode. The plasma is exposed to a magnetic field of 0.77 T. The discharge power is varying from (a) to (e). (a) 0.4 W, (b) 0.85 W, (c) 1.68 W, (d) 2.32 W, and (e) 4.03 W.

plasma density increases. With decreasing discharge power, the filamentary structures appear brighter and transition from continuous patterns to individual column filaments (bright spots when viewed from the top) at low discharge powers.

To study the effects of the plasma boundaries on filamentation, we repeated the experiments shown in Fig. 2, however, with a 2 mm thick glass plate (i.e., dielectric) placed on the lower electrode, effectively reducing the plasma boundary conductivity. As seen in Figs. 3(a)–3(e), this change results partly in the formation of more individual column filaments (bright spots when viewed from the top) but overall the filamentation smears out over a larger area and thus seems to be reduced at higher discharge powers compared to the case with aluminum (conducting) electrodes.

Finally, while still covering one electrode with a dielectric, we studied the influence of the neutral pressure for a constant discharge power of 1.38 W and a magnetic field of 0.77 T. Changing the pressure influences the ion–neutral collision mean-free path and the plasma density, both of which potentially have a strong effect on the filamentation state. These measurements, shown in Figs. 4(a)–4(e), are in good agreement with previously reported results in Ref. 38 and confirm that decreasing the pressure shifts the plasma toward forming more individual column filaments (bright spots when viewed from the top) while increasing the pressure results in the formation of continuous (target-like when viewed from the top) patterns in the plasma. The two observations are comparable even though in this work a glass plate was placed on the bottom electrode.

III. THE 3D FLUID MODEL

The experimental observations of filamentation in low-pressure and low-temperature discharges would benefit from computational modeling to aid in interpreting the experiments and determining the origin of the filaments. To this end, there have been recent two-dimensional (2D) simulations reported by Schweigert and Keidar[42] and Menati *et al.*[43] In Ref. 42, the formation of filamentary structures in a magnetized plasma is studied using a 2D kinetic model. In this model, neutral pressure is assumed to be very low (0.01 Pa) and the

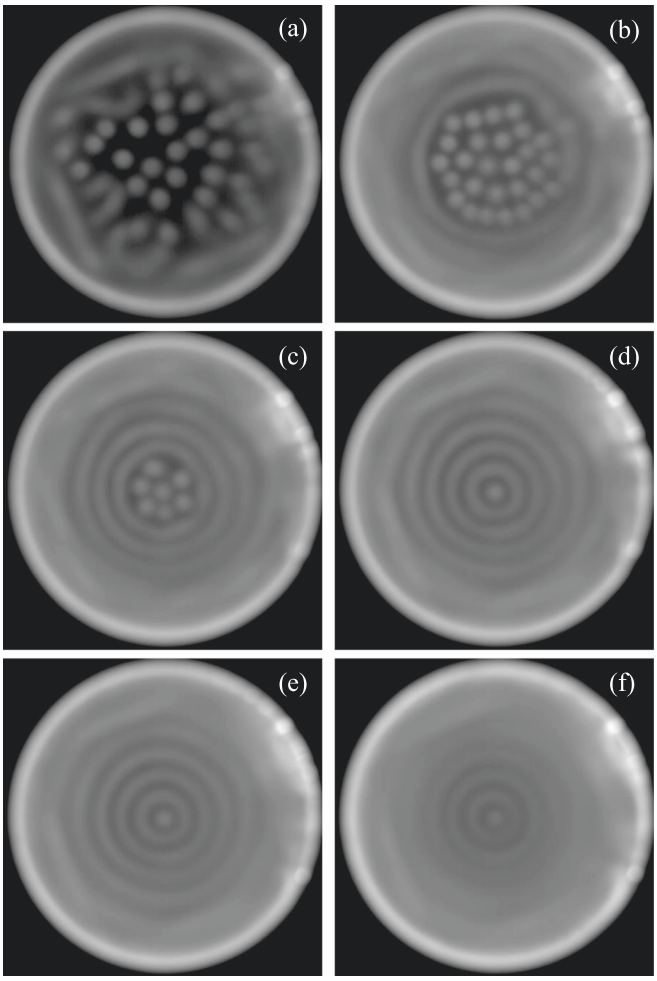

FIG. 4. The top view of pattern formation in an RF argon plasma at a discharge power of 1.38 W, magnetic field of 0.77 T, and different neutral gas pressures with a glass plate placed on the lower electrode. (a) 2.7 Pa, (b) 3.9 Pa, (c) 4.7 Pa, (d) 5.8 Pa, (e) 6.9 Pa, and (f) 8.4 Pa.

magnetic field (25–50 G) is oblique to the electrodes. Although the article presents a very good discussion on dependency of the filamentary structures on electron's Larmor radius and Debye length, the orientation of magnetic field with respect to the electrodes and the magnitudes of pressure and magnetic field in that article are not comparable to the experiments presented in the current work. Moreover, in Ref. 43, Menati *et al.* have investigated the dependency of the filamentary structures on the dielectric strength and secondary electron emission from the electrodes. Despite reviling some aspects of filamentation phenomenon, these two models were not able to fully capture the underlying physics behind the phenomenon. Therefore, to determine the nature of the observed filamentation instability, we developed a 3D numerical fluid model. The numerical model is intended to cover the dynamics of the electrons and ions, subject to neutral collisions, to understand how those dynamics could give rise to a filamentary structure in the plasma. The model will show how a density perturbation, in the form of a single column, aligned to the magnetic field direction, will form a series of filamentary structures parallel to the magnetic field.

A. Assumptions and base set of equations for the numerical model

The development of the model was influenced by choosing the minimum set of plasma transport equations that would address the phenomenon of filamentation while also being numerically efficient. The electric potential ϕ is obtained from the solution of Poisson's equation

$$\nabla^2\varphi = \frac{\rho}{\varepsilon}, \tag{2}$$

where ρ is the charge density given by $e(n_i - n_e)$ and ε is the electric permittivity that we have assumed to be constant throughout the plasmas. The dynamics of the plasma fluid elements of the individual species α (= e, i—for electrons and ions) are addressed by the fluid equation of motion

$$q_\alpha n_\alpha(\boldsymbol{E} + \boldsymbol{V}_\alpha \times \boldsymbol{B}) - \nabla \boldsymbol{P} - m_\alpha n_\alpha \upsilon_{\alpha-n}\boldsymbol{V}_\alpha = m_\alpha n_\alpha\left(\frac{\partial \boldsymbol{V}_\alpha}{\partial \boldsymbol{t}} + (\boldsymbol{V}_\alpha . \nabla)\boldsymbol{V}_\alpha\right), \tag{3}$$

where q_α is the charge, n_α is the density, $\boldsymbol{E}$ is the electric field vector given by $-\nabla\boldsymbol{\varphi}$, $\boldsymbol{V}_\alpha$ is the velocity vector, $\boldsymbol{B}$ is the magnetic field vector, P is the pressure, m_α is the mass, and $\upsilon_{\alpha\text{-}n}$ is the collision frequency with neutral atoms.

It is assumed that the background neutral gas is stationary and contributes to the plasma only through collisions with electrons and ions. We do not consider separate fluid equations for the neutrals, and we have not included excited states of the gas in the model. However, in a magnetized dusty plasma experiment, the rotation of the neutral atoms due to their collisions with the ions together with azimuthal ionic flow is responsible for the rotation of the dust particles in the magnetic field.[44,45] Additionally, in order to further simplify the model, the plasma is considered to be isothermal with no heat transfer, so we do not solve for electron/ion temperatures and assume that they are constant ($T_e = 2$ eV and $T_i = 0.025$ eV).[46–49] The plasma is sustained by a simple ionization model that will be discussed in detail later in this section.

Our experiments have shown that the dynamical time scale of the filamentary structures, once they are established, is on the order of seconds and thus much slower than the dynamics of electrons and ions. Therefore, for slow evolution of the phenomenon (steady state) and by neglecting acceleration and the nonlinear term on the right-hand side of Eq. (3), we get

$$q_\alpha n_\alpha(\boldsymbol{E} + \boldsymbol{V}_\alpha \times \boldsymbol{B}) - \nabla \boldsymbol{P} - m_\alpha n_\alpha \upsilon_{\alpha-n}\boldsymbol{V}_\alpha = 0. \tag{4}$$

The flux of each species, (Γ_α), is then given by

$$\Gamma_\alpha = n_\alpha \boldsymbol{V}_\alpha. \tag{5}$$

Also, the collision frequencies are calculated using the following equation:

$$\upsilon_\alpha = n_g \sigma_\alpha V_{th} \tag{6}$$

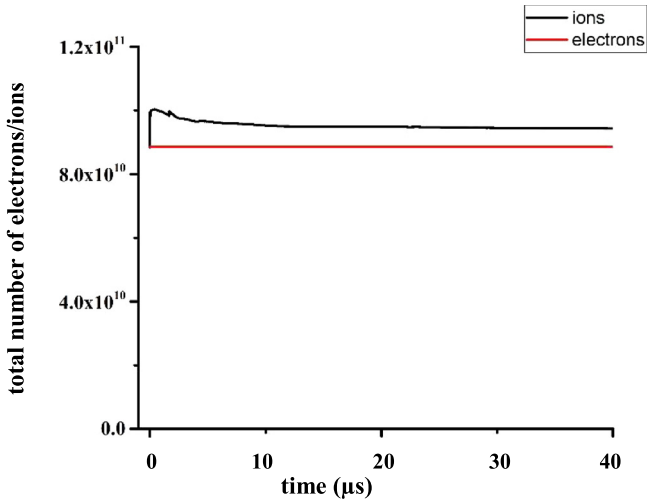

FIG. 5. Total number of electrons (red line) and ions (black line) in the simulation over time.

in which n_g is the neutral gas density, σ_α is the electron/ion collision cross section with neutral atoms, and V_{th} is the electron/ion average thermal velocity. All collision cross sections are obtained from recent resources.[50–52]

Finally, we solve the continuity equation that governs the relation between the plasma fluxes and the local densities including the sources and the losses

$$\frac{\partial n_\alpha}{\partial t} + \nabla \cdot \Gamma\alpha = \sigma_I - \sigma_L \tag{7}$$

in which σ_I and σ_L are ionization and recombination rates, respectively.

Unlike Eq. (4), we keep the time derivative term in continuity equation to cover the slow dynamics of the plasma filamentation. Without the time derivative in Eq. (7), the whole model will be time independent and we cannot investigate the time evolution of the pattern formation in the plasma. This approach has been employed in plasma simulation for a long time.[53–61] As our systems are weakly ionized, ionization fraction on the order of 10^{-6} to 10^{-8}, electron–ion and electron–electron collisions are neglected. In solving Eq. (7), therefore, we assume that electron–ion recombination only takes place on the surfaces of the discharge while ionization occurs only in the bulk of the plasma. That is, there is no secondary electron emission from the walls of the chamber. If the total number of the lost particles at the walls for a given time interval is assumed to be S_L, and the total number of electrons is S_i, our ionization model reads

$$\gamma = \frac{S_L}{S_I - S_L}, \tag{8}$$

$$\sigma_I = \gamma n_e(x, y, z). \tag{9}$$

With electrons and ions produced at the same rate proportional to the local electron density, the continuity equation in the bulk of the plasma becomes

$$\frac{\partial n_\alpha}{\partial t} + \nabla \cdot \Gamma\alpha = \gamma n_e(x, y, z). \tag{10}$$

The loss of electrons to the walls is more than the ions due to their smaller mass and higher mobility. Therefore, in order to sustain the

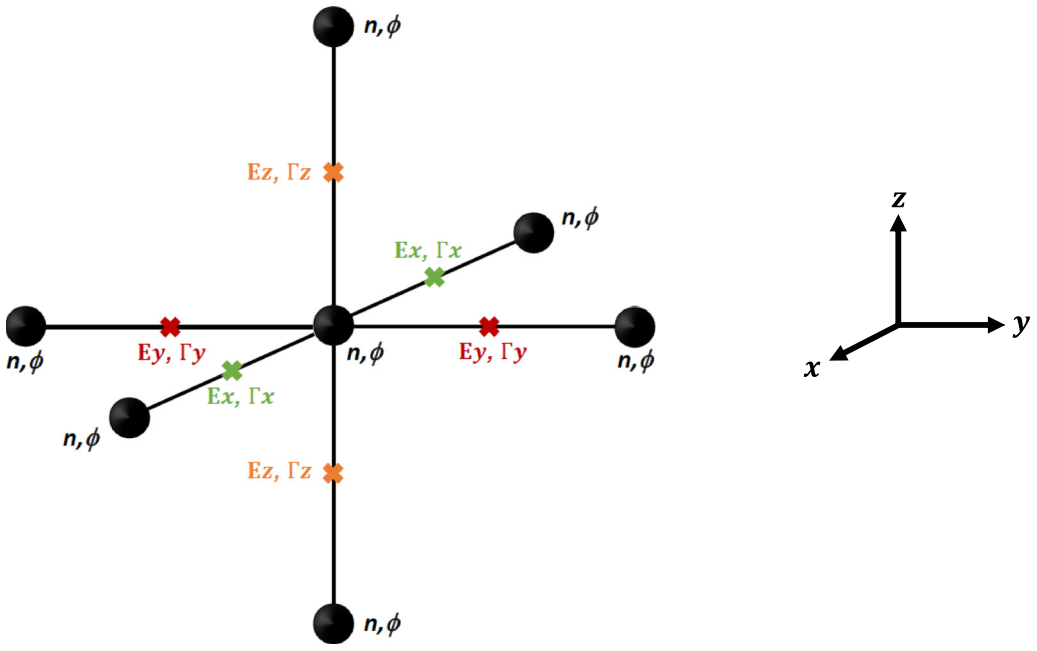

FIG. 6. The multimesh computational grid. The electric potential and electron/ion densities are calculated on the main grid points (black circles), while the electric field and electron/ion fluxes are obtained at the corresponding midpoints.

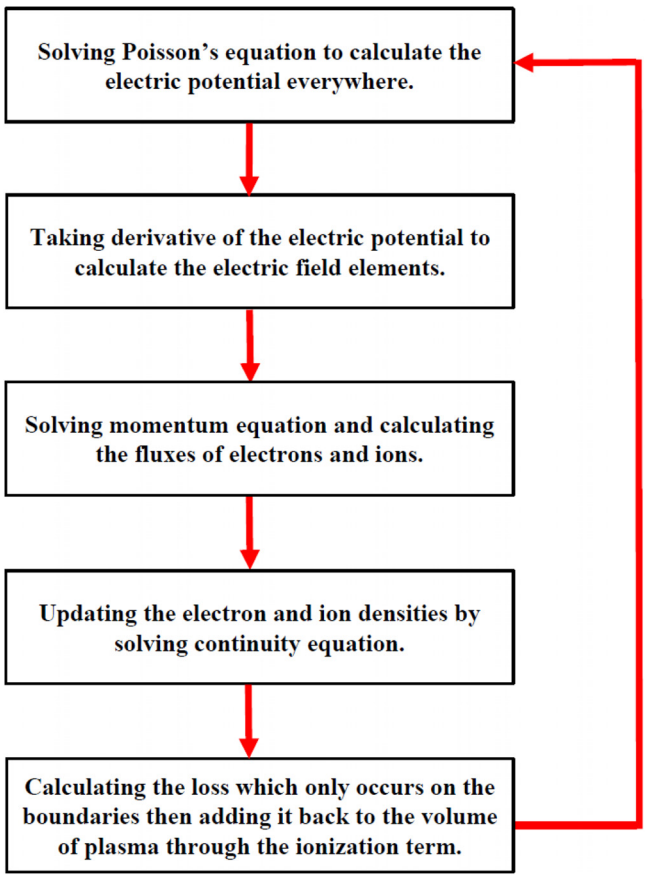

FIG. 7. The simulation algorithm.

plasma in our simulation, we keep the overall number of electrons constant by replacing any losses of electrons to the walls. For each ionization process, an electron/ion pair at their target temperatures ($T_e = 2$ eV and $T_i = 0.025$ eV) is added to the bulk of the plasma. It has to be mentioned that, in this ionization model, the total number of the ions added to the plasma in each cycle of the simulation is more than the number of ions lost at the walls but this slight excess of ions will eventually diffuse toward the walls and equilibrium will be reached. To show that equilibrium will be reached through this model, the total number of electrons and ions in the simulation as a function of time is depicted in Fig. 5.

B. Algorithm and computational space

We have used a 3D multimesh configuration to simulate a rectangular plasma chamber with metal walls on all sides. As shown in Fig. 6, the electric potential and electron/ion densities are calculated on the main mesh points (black circles in Fig. 6), while electric field and electron/ion fluxes are derived at midpoints between two main mesh points in the X, Y, and Z direction. Since the fluxes and the dynamic of the charged species parallel to the magnetic field will not be affected by the magnetic field, the mesh spacing in this direction is considered larger than the spacing perpendicular to the magnetic field. This is computationally beneficial, resulting in a reduction of the total number of grid points.

The successive over-relaxation (SOR) method[62] is employed to solve Poisson's equation with the boundary condition of zero potential at the metal walls. The electric field at the midpoints is then calculated from the potential, which will be plugged in the momentum equation to evaluate the electron/ion fluxes at halfway between the main mesh points. A fourth order Runge-Kutta method is used to evaluate continuity equation, Eq. (10), and update electron and ion densities on the grid. The last step of one simulation loop is now complete and the simulation has advanced one step in time. The overall simulation algorithm is depicted in Fig. 7. The equations are solved using a graphics processing unit (GPU) parallel code using NVIDIA CUDA[63] to accelerate the simulation.

C. Simulation results reproducing the experimental findings

It has to be mentioned that typical electron density and temperature in the MDPX device at $B = 0$ are $4–10 \times 10^{14}$ m^{-3} and 2–4 eV, respectively, and there is no reliable probe theory to measure theses quantities in the magnetized plasma. Therefore, a uniform argon plasma at a background electron/ion density of 5×10^{14} m^{-3} is considered in the simulation. The electron and ion temperatures are initialized at 2 and 0.025 eV, respectively, and are assumed to be constant. The volume of the simulated plasma is $6.3 \times 6.3 \times 4.2$ cm^2. The spatial step-size is set to 3.5×10^{-4} m in the X/Y direction (perpendicular to the magnetic field) and 6×10^{-4} m in the z direction (parallel to the magnetic field), which are a fraction of the Debye length which is ~1 mm for the selected plasma density and temperature values. Since our simulation is explicit, to avoid numerical instabilities, we have used a simulation time step of 10^{-11} s to ensure that the time step is not larger than the dielectric relaxation time of the plasma[64]

$$\Delta t_d = \frac{\varepsilon_0}{\sigma}, \tag{11}$$

where σ is the plasma conductivity. Since the time step in the simulation is very small and the dynamics of the filaments in the experiments occur at time scales on the order of milliseconds to seconds, currently it is not feasible to simulate the dynamic of the filaments in the

TABLE I. Typical length and time scale in the simulation. In this table, Δx is the step size in the x and y direction, λ_{De} is the electron Debye length, r_{Li} is the ion Larmor radius, λ_i is the ion mean-free-path, L_x is the length of the plasma chamber in the X and Y direction, Δt is the time step, ω_{pe} is the electron plasma frequency, ω_{ci} is the ion gyrofrequency, υ_i is the ion collision frequency, and t_f the is typical time scale for the motion of filaments with respect to each other in the experiments.

$\Delta x = 3.5 \times 10^{-4}$ m	$\lambda_{De} = 5.2 \times 10^{-4}$ m	$r_{Li} = 2.5 \times 10^{-4}$ m	$\lambda_i = 7.3 \times 10^{-4}$ m	$L_x \approx 6$ cm
$\Delta t = 1 \times 10^{-11}$ s	$\frac{1}{\omega_{pe}} = 9.1 \times 10^{-10}$ s	$\frac{1}{\omega_{ci}} = 2.1 \times 10^{-7}$ s	$\frac{1}{\upsilon_i} = 1.3 \times 10^{-6}$ s	$t_f \approx 1$ ms–1 s

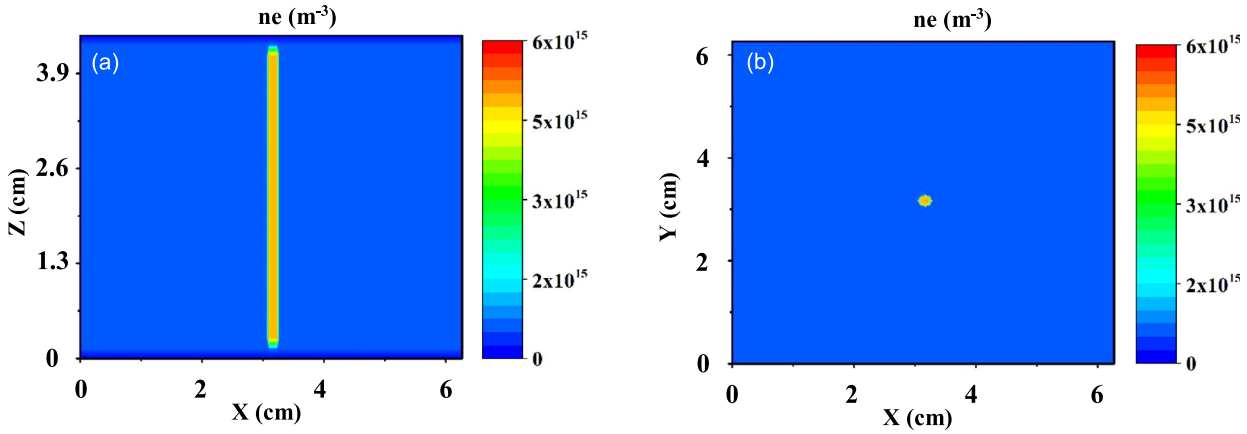

FIG. 8. Cross section of initial electron density at $t = 0$ s. (a) side view ($Y = 3.2$ cm), (b) top view ($Z = 2.1$ cm).

chamber with respect to each other. Table I presents the typical length and time scales for the plasma parameters mentioned above.

To trigger the pattern formation, it is obvious that some form of perturbation is needed. Therefore, we arbitrarily chose to introduce a high density plasma column along the z-direction (parallel to the magnetic field), with $n_e = n_i = 5 \times 10^{15}$ m^{-3} to break the initial homogeneity of the background plasma. Although we have considered the perturbation to be 10 times the background density, a smaller

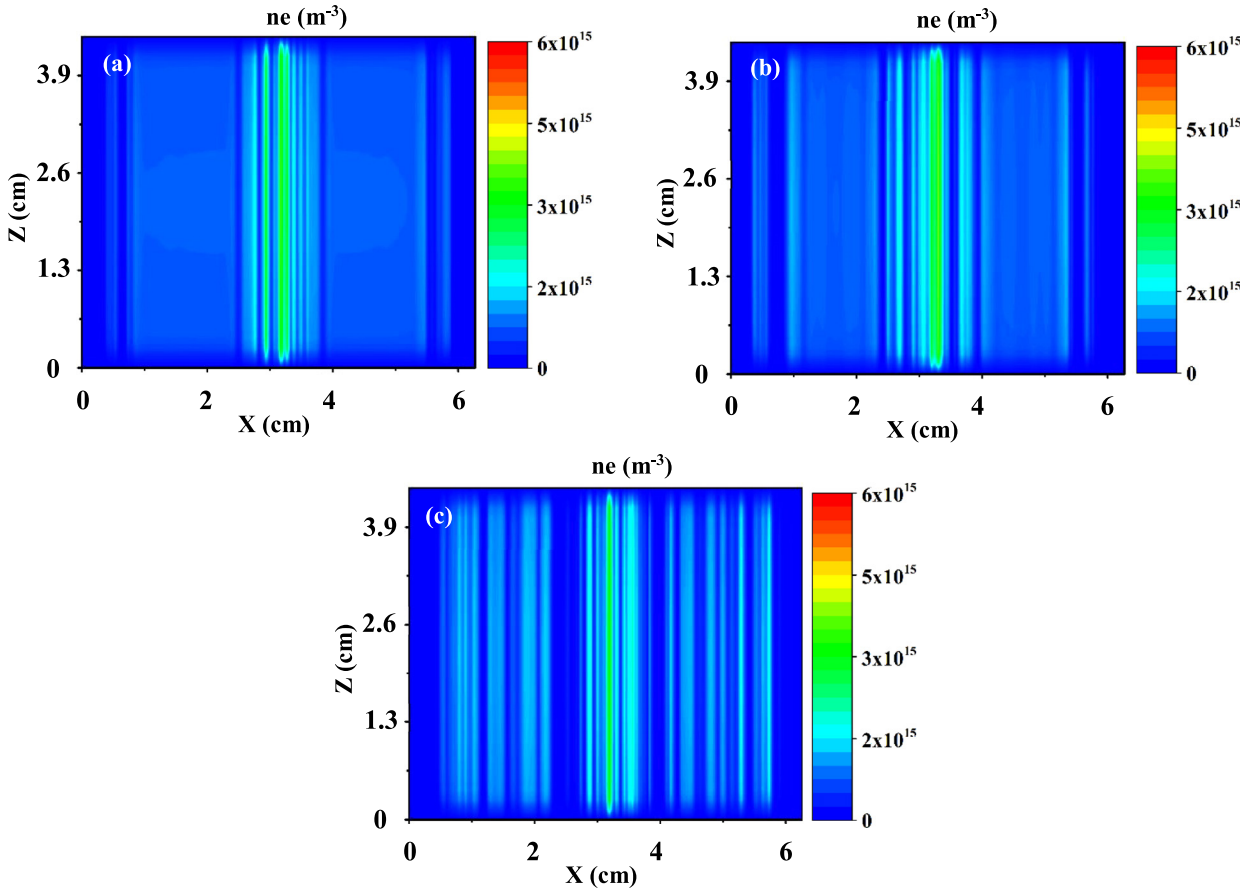

FIG. 9. Side view of the time evolution of pattern formation in the plasma at pressure $p = 10$ Pa and magnetic field $B = 1$ T. (a) $t = 20$ μs, (b) $t = 30$ μs, and (c) $t = 40$ μs.

perturbation would give the same results but the smaller the initial perturbation, the longer it takes for the patterns to appear in the plasma. In the simulations presented in this work, the introduced inhomogeneity in the plasma (the enhanced plasma density column along B) has a diameter of 2 mm, as depicted in Fig. 8 for $t = 0$ s.

Simulations are performed under variation of pressure, plasma density (power), and gas type to compare the results with experimental observations in the current Letter and those presented in Refs. 37–40. In all of these cases, the plasma structures are in the X-Y plane across B, while along B (Z direction) the density behaves like a one dimensional plasma as it is displayed in a representative case in Fig. 9. This is also in good agreement with the side view pictures of filamentation presented in Ref. 38. Further, we only look at the pattern formation as seen from the top (X-Y plane cross section at $Z = 2.1$ cm) and our simulations are stopped at the same time $t = 40$ μs (4×10^6 time steps of simulation). The filamentary structures are fully formed in the simulation at this time and their shapes do not significantly change after this time. The experimental time scales of the formation of the filamentary structures need very high speed cameras and are beyond the scope of this work.

In Fig. 10, the X-Y cross section of the electron density profile of the plasma at the center of the chamber is presented for three different pressures while keeping the background magnetic field at $B = 1$ T. The plasma density was kept constant too, at the value of 5×10^{14} m^{-3}. It should be noted that this is usually not possible in an experiment as a pressure change also induces a plasma density change. The simulation results confirm the general observation that the filamentary patterns appear in a magnetized plasma at lower pressures (typical pressures $P < 20$ Pa for $B = 1$ T), while they are suppressed and the plasma becomes homogeneous at higher pressures (typical pressures $P \geq 20$ Pa for $B = 1$ T). For comparison see the experimental results presented in Fig. 4 and observations in Refs. 37–40. The ion density and plasma potential profiles also follow the same patterns as the electron density and are therefore not shown here.

Moreover, the continuous patterns formed in this simulation are rectangular closer to the walls and more curved in the center of the discharge, suggesting that the rectangular boundary condition in this simulation is imposing its shape to the filamentary patterns. It is noted that for the images shown in Figs. 2–4, a circular ring was placed on the electrode which may be enforcing the observed circular patterns.

In addition to that, the whole plasma rotates due to the presence of magnetic field as it was also observed in the experiments. The flow of the plasma along the walls and the strong electric field due to the plasma sheath in that region result in instabilities such as

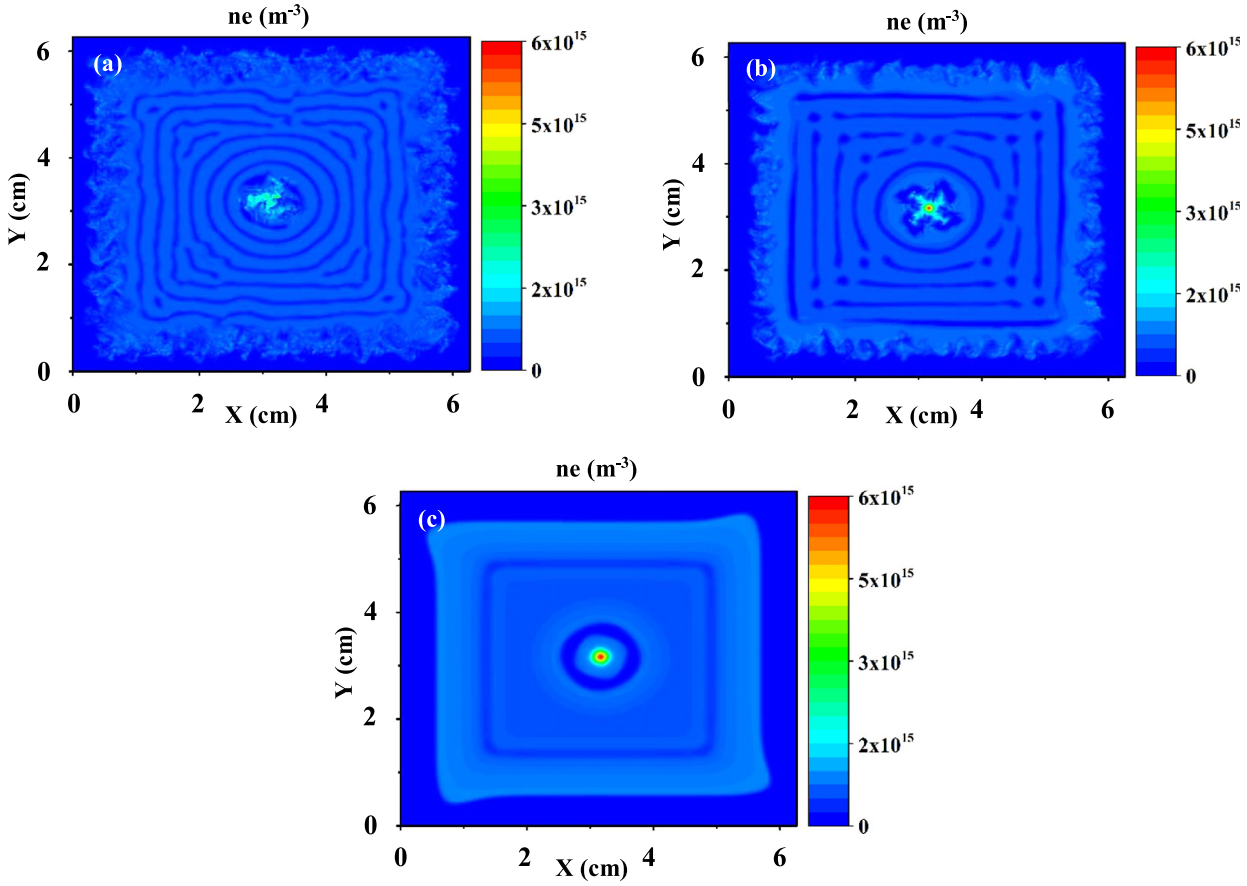

FIG. 10. X-Y cross section of electron density at $t = 40$ μs for different pressures in the presence of 1 T magnetic field. (a) $p = 5$ Pa, (b) $p = 10.0$ Pa, and (c) $p = 20.0$ Pa.

Kelvin–Helmholtz and Rayleigh–Taylor instabilities which are responsible for the roughness of the plasma near the walls. These instabilities are suppressed at higher pressures due to neutral collisions as it can be noticed in Fig. 9(c).

The change in the pattern formation by changing the plasma density at a constant gas pressure of 10 Pa is shown in Fig. 11. This is equivalent of changing discharge power in an experiment. When increasing the plasma density, first the filamentary patterns get narrower and closer to one another, then they form unorganized filamentary structures, and finally the patterns disappear at higher plasma densities. These results are also qualitatively in agreement with experimental observation presented in Figs. 2 and 3. The electron Debye length ($\lambda_{De} = \sqrt{\frac{\varepsilon_0 K_B T_e}{q_e^2 n_e}}$, where K_B is Boltzmann's constant and T_e is electron temperature) depends on the electron density, and the fact that its variation can affect the configuration of the filamentary structure shows that the electron Debye length is also an important factor in the filamentation phenomenon.

Finally, the formation of patterns in different gas types (Ne, Ar, Kr) at a constant plasma density of 5×10^{14} m^{-3}, pressure of 10 Pa, and $B = 1$ T is shown in Fig. 12. The filamentary patterns appear in the plasma for lighter ions but for the heavier ions, they tend to disappear and plasma becomes smoother. The current work is not focused on quantitative description of the filamentation phenomenon and that aspect of the phenomenon will be discussed in a future article. Since the collision cross sections for heavier atoms are higher, the ion–neutral collision mean-free-path will be shorter for heavier atoms at the same electron/ion temperatures. The mass of the ions also affects the ion gyroradius, suggesting that the dynamics of the ions is an important factor in the formation and characteristics of the patterns which was also pointed out by Schwabe *et al.* in Ref. 38.

The results displayed in Fig. 12 along with other simulations presented in the current work revealed that the three characteristic lengths of electron/ion Debye length, ion mean-free-path, and ion gyroradius play an important role in the filamentation of the magnetized plasmas. For magnetic fields on the order $B \geq 1$ T, the electrons are strongly magnetized and their diffusion is primarily parallel to the magnetic field. On the other hand, although ions also diffuse mainly parallel to the magnetic field, they still have a limited diffusion across the magnetic field with the help of their larger mass which results in a

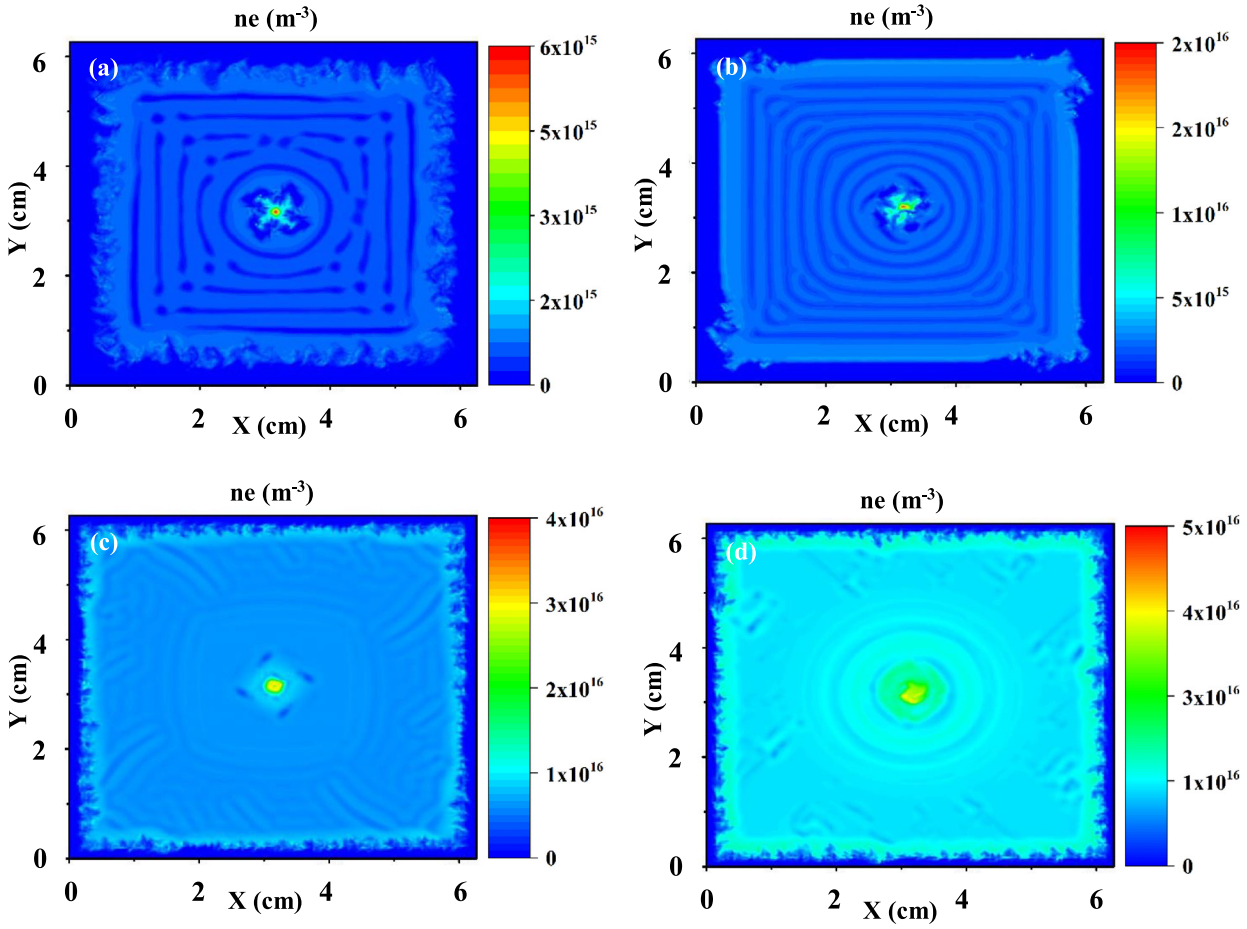

FIG. 11. X-Y cross section of electron density, $\mathbf{n_e}$, at $t = 40$ μs for different electron densities in the presence of 1 T magnetic field. (a) $n_e = 5 \times 10^{14}$ m^{-3}, (b) $n_e = 10^{15}$ m^{-3}, (c) $n_e = 5 \times 10^{15}$ m^{-3}, and (d) $n_e = 10^{16}$ m^{-3}.

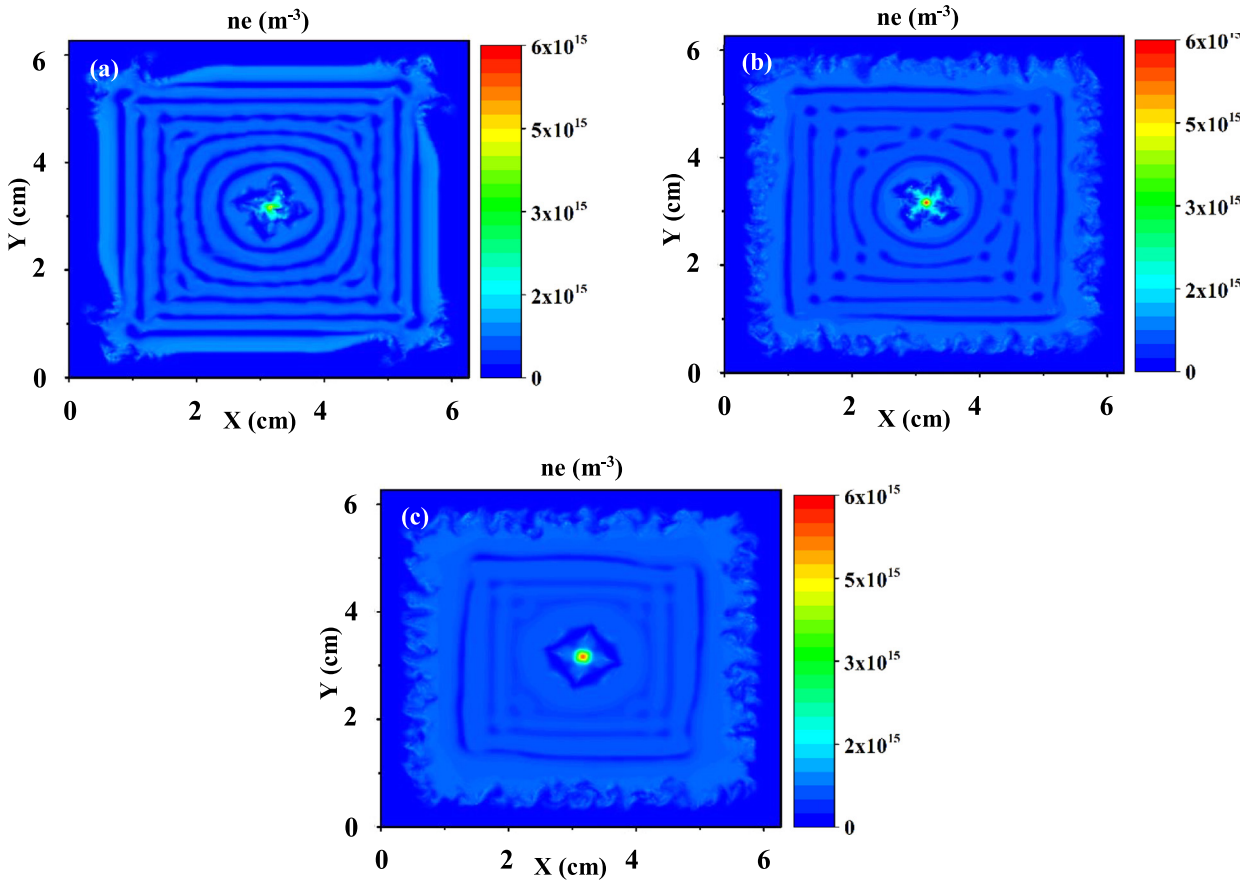

FIG. 12. Pattern formation in Ne and Kr at plasma density of 10^{14} m^{-3} and pressure of 10 Pa exposed to 1 T magnetic field. (a) Ne, (b) Ar, and (c) Kr.

nonambipolar diffusion mechanism in strongly magnetized plasmas.[65] Among the three characteristic lengths mentioned above, the Debye length is an important factor in the diffusion of the electrons and ions parallel to the magnetic field and the ions' mean-free-path and gyroradius affect the cross magnetic field diffusion of the ions.[65] Therefore, the nonambipolar diffusion of the electrons and ions in magnetized plasmas is mainly controlled by these characteristic lengths. This nonambipolar diffusion (as compared to ambipolar diffusion in nonmagnetized plasmas) is the main consequence of the applied magnetic field and therefore may be responsible for the filamentation phenomenon. Further investigation is needed to study the detail of this hypothesis more precisely which will be the subject of future works.

IV. SUMMARY

The effects of power deposition, neutral pressure variations, and electrode conductivity were investigated experimentally on the behavior of filamentary pattern formation in a plasma under the influence of a strong magnetic field. In addition, we have set up a self-consistent, three-dimensional fluid simulation model that allowed us to study the observed filamentation instability in more details. Simulations were performed with the goal to reproduce the observation and to study dependencies that are not accessible in the experiment. We could validate that increasing pressure and increasing molecular weight results in a decrease in the filamentary strength consistent with the experimental observations from this paper and Refs. 37–40. Our simulations were further able to study the dependency of the plasma density alone, which was not possible in any so far performed experiments. The results indicate that beyond the assumed influence of the ion–neutral collision mean-free-path and the Larmor radius, a third parameter, the Debye length, might play an important role. The latter was not yet considered in earlier, experiment driven works. Overall, the performed simulations were able to shine a new light on the physical influences that cause the here investigated structures.

Additional experiments and specifically detailed simulation are necessary to explore if parameters, beyond the mean-free-path, Larmor radius and Debye length such as the geometry of the chamber can affect the filamentary instability. Through this work, it was proposed that the filamentation phenomenon might be an outcome of nonambipolar diffusion mechanisms in magnetized plasmas. Simulations are specifically suitable since, different than in the experiment, they allow to investigate the influence of individual parameters one-by-one. For instance, pattern formation in thermalized plasmas ($T_e = T_i$) can be studied which might have an impact on plasma environments such as space plasmas (solar prominence and solar protuberances) and fusion plasma. Discovering the underlying physics would allow us to derive an analytical description and potentially give

an insight into pattern formation and self-organization for other environments which are governed by a similar set of equations. Potential environments include those based on anisotropic heat transfer.

ACKNOWLEDGMENTS

The authors would like to thank Professor Mark Kushner for his thoughtful comments and Doctor Bryan Lynch for his contribution to the experimental measurements. This work was supported by funds from the National Science Foundation EPSCoR programme (No. OIA-1655280) and U.S. Department of Energy (No. SC-0016330).

REFERENCES

[1]M. Cross and H. Greenside, *Pattern Formation and Dynamics in Nonequilibrium Systems* (Cambridge University Press, Cambridge, 2009).
[2]M. Rietkerk and J. van de Koppel, Trends Ecol. Evol. **23**, 169 (2008).
[3]H. Meinhardt, J. Mar. Biol. Assoc. U.K. **75**, 1004 (1995).
[4]B. Liebchen, D. Marenduzzo, I. Pagonabarraga, and M. E. Cates, Phys. Rev. Lett. **115**, 258301 (2015).
[5]K. Agladze, L. Budriene, G. Ivanitsky, V. Krinsky, V. Shakhbazyan, and M. Tsyganov, Proc. R. Soc. London, Ser. B **253**, 131 (1993).
[6]V. V. Bel'kov, J. Hirschinger, V. Novák, F.-J. Niedernostheide, S. D. Ganichev, and W. Prettl, Nature **397**, 398 (1999).
[7]R. Kapral, Physica D **86**, 149 (1995).
[8]P. Drazin and J. Crepeau, Appl. Mech. Rev. **56**, B43 (2003).
[9]R. D. Deegan, Phys. Rev. E **61**, 475 (2000).
[10]K. C. Wali, in *A Quest Perspective* (Imperial College Press, 2001), pp. 531–649.
[11]H. Brandtstädter, M. Braune, I. Schebesch, and H. Engel, Chem. Phys. Lett. **323**, 145 (2000).
[12]F. G. Baksht, G. A. Dyuzhev, N. K. Mitrofanov, and S. M. Shkol'nik, Tech. Phys. **42**, 35 (1997).
[13]S. Zhang and T. Dufour, Phys. Plasmas **25**, 073502 (2018).
[14]G. Yang and J. Heberlein, Plasma Sources Sci. Technol. **16**, 765 (2007).
[15]D. Schuocker, IEEE Trans. Plasma Sci. **7**, 209 (1979).
[16]M. Wagner, A. Kohut, Z. Geretovszky, M. Seipenbusch, and G. Galbács, J. Aerosol. Sci. **93**, 16 (2016).
[17]G. A. Dyuzhev, G. A. Lyubimov, and S. M. Shkol'Nik, IEEE Trans. Plasma Sci. **11**, 36 (1983).
[18]M. S. Benilov, Phys. Rev. E **77**, 036408 (2008).
[19]H.-G. Purwins, H.-J. Hartfuss, M. Dudeck, J. Musielok, and M. J. Sadowski, AIP Conf. Proc. **993**, 67–74 (2008).
[20]K. H. Schoenbach, M. Moselhy, and W. Shi, Plasma Sources Sci. Technol. **13**, 177 (2004).
[21]U. Ebert, W. van Saarloos, and C. Caroli, Phys. Rev. Lett. **77**, 4178 (1996).
[22]U. Ebert and M. Arrayás, *Pattern Formation in Electric Discharges* (Springer, 2001), pp. 270–282.
[23]B. Li and J. Ouyang, Phys. Plasmas **23**, 113509 (2016).
[24]L. F. Dong, W. L. Fan, S. Wang, Y. F. Ji, Z. W. Liu, and Q. Chen, Phys. Plasmas **18**, 033506 (2011).
[25]S. N. Abolmasov, T. Shirafuji, and K. Tachibana, IEEE Trans. Plasma Sci. **33**, 941 (2005).
[26]A. Chirokov, A. Gutsol, A. Fridman, K. D. Sieber, J. M. Grace, and K. S. Robinson, Plasma Chem. Plasma Process. **26**, 127 (2006).
[27]J. P. Trelles, J. Phys. D: Appl. Phys. **49**, 393002 (2016).
[28]G. I. Kent, Phys. Fluids **12**, 2140 (1969).
[29]Y. Amagishi, Y. Yoshikawa, and J. Ohara, J. Phys. Soc. Jpn. **60**, 2496 (1991).
[30]T. Ikehata, H. Tanaka, N. Y. Sato, and H. Mase, Phys. Rev. Lett. **81**, 1853 (1998).
[31]C. F. Driscoll, D. A. Schecter, D. Z. Jin, D. H. E. Dubin, K. S. Fine, and A. C. Cass, Physica A **263**, 284 (1999).
[32]R. Keppens, G. Tóth, R. H. J. Westermann, and J. P. Goedbloed, J. Plasma Phys. **61**, 1 (1999).
[33]M. Kono and M. Y. Tanaka, Phys. Rev. Lett. **84**, 4369 (2000).
[34]M. Kono, H. L. Pécseli, and J. Trulsen, Phys. Scr. **61**, 489 (2000).
[35]J. P. Trelles, Plasma Sources Sci. Technol. **22**, 025017 (2013).
[36]J. P. Trelles, Plasma Sources Sci. Technol. **23**, 054002 (2014).
[37]U. Konopka, AIP Conf. Proc. **799**, 181–184 (2005).
[38]M. Schwabe, U. Konopka, P. Bandyopadhyay, and G. E. Morfill, Phys. Rev. Lett. **106**, 215004 (2011).
[39]P. Bandyopadhyay, D. Sharma, U. Konopka, and G. Morfill, AIP Conf. Proc. **1582**, 281–287 (2014).
[40]E. Thomas, U. Konopka, R. L. Merlino, and M. Rosenberg, Phys. Plasmas **23**, 055701 (2016).
[41]E. Thomas, R. L. Merlino, and M. Rosenberg, Plasma Phys. Controlled Fusion **54**, 124034 (2012).
[42]I. V. Schweigert and M. Keidar, J. Phys. Conf. Ser. **927**, 012048 (2017).
[43]M. Menati, E. Thomas, and M. J. Kushner, Phys. Plasmas **26**, 063515 (2019).
[44]J. Carstensen, F. Greiner, L.-J. Hou, H. Maurer, and A. Piel, Phys. Plasmas **16**, 013702 (2009).
[45]A. R. Abdirakhmanov, Z. A. Moldabekov, S. K. Kodanova, M. K. Dosbolayev, and T. S. Ramazanov, IEEE Trans. Plasma Sci. **47**, 3036 (2019).
[46]S. Nunomura, N. Ohno, and S. Takamura, Jpn. J. Appl. Phys., Part 1 **36**, 877 (1997).
[47]Y. Tomita, R. Smirnov, and S. Zhu, Plasma Sci. Technol. **7**, 2657 (2005).
[48]N. Sternberg, V. Godyak, and D. Hoffman, Phys. Plasmas **13**, 063511 (2006).
[49]A. R. Niknam, T. Haghtalab, and S. M. Khorashadizadeh, Phys. Plasmas **18**, 113707 (2011).
[50]L. C. Pitchford, L. L. Alves, K. Bartschat, S. F. Biagi, M. C. Bordage, A. V. Phelps, C. M. Ferreira, G. J. M. Hagelaar, W. L. Morgan, S. Pancheshnyi, V. Puech, A. Stauffer, and O. Zatsarinny, J. Phys. D: Appl. Phys. **46**, 334001 (2013).
[51]M. C. Bordage, S. F. Biagi, L. L. Alves, K. Bartschat, S. Chowdhury, L. C. Pitchford, G. J. M. Hagelaar, W. L. Morgan, V. Puech, and O. Zatsarinny, J. Phys. D: Appl. Phys. **46**, 334003 (2013).
[52]L. L. Alves, K. Bartschat, S. F. Biagi, M. C. Bordage, L. C. Pitchford, C. M. Ferreira, G. J. M. Hagelaar, W. L. Morgan, S. Pancheshnyi, A. V. Phelps, V. Puech, and O. Zatsarinny, J. Phys. D: Appl. Phys. **46**, 334002 (2013).
[53]D. B. Graves and K. F. Jensen, IEEE Trans. Plasma Sci. **14**, 78 (1986).
[54]Y. Oh, N. Choi, and D. Choi, J. Appl. Phys. **67**, 3264 (1990).
[55]M. H. Wilcoxson and V. I. Manousiouthakis, IEEE Trans. Plasma Sci. **21**, 213 (1993).
[56]A. Bogaerts, R. Gijbels, and W. J. Goedheer, J. Appl. Phys. **78**, 2233 (1995).
[57]H. Akashi, Y. Sakai, N. Takahashi, and T. Sasaki, J. Phys. D: Appl. Phys. **32**, 2861 (1999).
[58]S. Medina, K. Yanallah, L. Mehdaoui, A. Belasri, and T. Baba-Hamed, Plasma Devices Oper. **13**, 1 (2005).
[59]A. Derzsi, P. Hartmann, I. Korolov, J. Karácsony, G. Bánó, and Z. Donkó, J. Phys. D: Appl. Phys. **42**, 225204 (2009).
[60]T. Samir, Phys. Plasmas **21**, 083511 (2014).
[61]S. I. Eliseev, E. A. Bogdanov, and A. A. Kudryavtsev, Phys. Plasmas **24**, 093503 (2017).
[62]M. A. Onabid, Afr. J. Math. Comput. Sci. Res. **5**, 204 (2012).
[63]J. Nickolls, I. Buck, M. Garland, and K. Skadron, Queue **6**, 40 (2008).
[64]M. S. Barnes, T. J. Cotler, and M. E. Elta, J. Comput. Phys. **77**, 53 (1988).
[65]F. F. Chen, *Introduction to Plasma Physics and Controlled Fusion* (Springer, Boston, MA, 1984).